Comparison of the polynomial model against explicit measurements of noise components for different mammography systems

2014 Phys. Med. Biol. 59 5741

(http://iopscience.iop.org/0031-9155/59/19/5741)

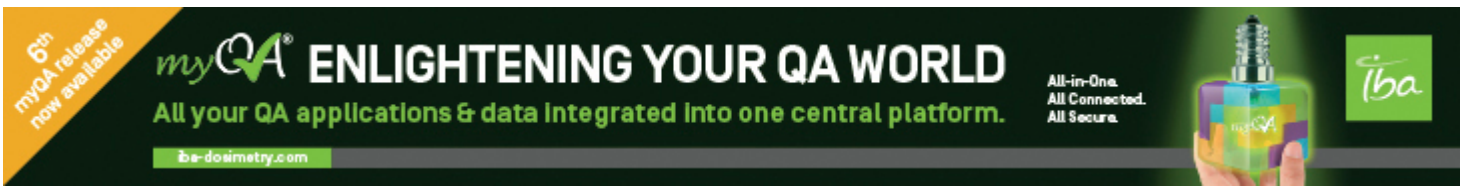

IOP Publishing | Institute of Physics and Engineering in Medicine Physics in Medicine & Biology

Phys. Med. Biol. **59** (2014) 5741–5761 doi:10.1088/0031-9155/59/19/5741

Comparison of the polynomial model against explicit measurements of noise components for different mammography systems

P Monnin[1,3], H Bosmans[2], F R Verdun[1] and N W Marshall[2]

[1] Institute of radiation physics (IRA), Lausanne University Hospital (CHUV), Rue du Grand-Pré 1, 1007 Lausanne, Switzerland
[2] UZ Gasthuisberg, Medical Imaging Research Center & Department of Radiology, Herestraat 49, 3000 Leuven, Belgium
[3] Haute Ecole de Santé Vaud (HESAV), Filière TRM, Avenue de Beaumont 21, 1011 Lausanne, Switzerland

E-mail: pascal.monnin@chuv.ch

Received 27 February 2014, revised 4 August 2014
Accepted for publication 6 August 2014
Published 8 September 2014

Abstract

Given the adverse impact of image noise on the perception of important clinical details in digital mammography, routine quality control measurements should include an evaluation of noise. The European Guidelines, for example, employ a second-order polynomial fit of pixel variance as a function of detector air kerma (DAK) to decompose noise into quantum, electronic and fixed pattern (FP) components and assess the DAK range where quantum noise dominates. This work examines the robustness of the polynomial method against an explicit noise decomposition method. The two methods were applied to variance and noise power spectrum (NPS) data from six digital mammography units. Twenty homogeneously exposed images were acquired with PMMA blocks for target DAKs ranging from 6.25 to 1600 μGy. Both methods were explored for the effects of data weighting and squared fit coefficients during the curve fitting, the influence of the additional filter material (2 mm Al versus 40 mm PMMA) and noise de-trending. Finally, spatial stationarity of noise was assessed.

Data weighting improved noise model fitting over large DAK ranges, especially at low detector exposures. The polynomial and explicit decompositions generally agreed for quantum and electronic noise but FP noise fraction was consistently underestimated by the polynomial method. Noise decomposition as a function of position in the image showed limited noise stationarity, especially for FP noise; thus the position of the region of interest (ROI) used for noise decomposition may influence fractional noise

composition. The ROI area and position used in the Guidelines offer an acceptable estimation of noise components. While there are limitations to the polynomial model, when used with care and with appropriate data weighting, the method offers a simple and robust means of examining the detector noise components as a function of detector exposure.

Keywords: mammography, image quality assessment, noise decomposition

(Some figures may appear in colour only in the online journal)

1. Introduction

Image noise is a vital concept when describing the quality of mammography images and has been shown to obscure object detectability (Saunders *et al* 2007, Warren *et al* 2012). In radiological imaging, image noise can be considered to be composed of two principal components: 'anatomical noise' arising from patient structures and 'system noise' due to the physical nature of the imaging system. System noise has been characterized in numerous studies, from theoretical analysis of noise sources in x-ray imaging systems (Barnes 1982, Rabbani *et al* 1987, Nishikawa and Yaffe 1990, Hajdok *et al* 2006) to practical assessment of noise (Scheibe and Thomas 1981, Hillen *et al* 1987, Williams *et al* 1999, Evans *et al* 2002, Borasi *et al* 2003, Burgess 2004, Mackenzie and Honey 2007, Al Thali *et al* 2009, Bouwman *et al* 2009). This work implements an exhaustive procedure to accurately measure the noise components with the aim of evaluating the polynomial method for noise characterization and follow-up during QC in digital mammography (Perry *et al* 2013).

The three noise sources associated with digital x-ray imaging systems are electronic, x-ray quantum and fixed pattern (FP) noise. These noise components can be analyzed using variance (standard deviation) and by noise power spectrum (NPS). Both Borasi *et al* (2003) and Burgess (2004) apply the second order polynomial model to the variance measured in an image and expressed as a function of detector exposure. Bouwman *et al* (2009) have applied this model to a number of digital mammography systems and this method now constitutes part of the quality assurance measurements prescribed in the European Guidelines (EC 2006, Perry *et al* 2013) for digital mammography. An analogous approach can be applied to the NPS to derive the electronic, quantum and fixed pattern NPS (Mackenzie and Honey (2007), Al Thali *et al* (2009)). The accuracy of the model for quantifying electronic, quantum and fixed pattern noise components has however not been compared against other approaches. In this work, we verify the second-order polynomial model against an explicit noise separation in which non-stochastic noise is used to quantify FP noise. The FP noise component can be explicitly separated using a set of many images acquired at a given exposure level to form an average image which is then divided or subtracted from the image set, as described by Granfors and Aufrichtig (2000) for a digital radiography (DR) detector and by Illers *et al* (2004) for a computed radiography (CR) system. In addition, the influence of the following factors on noise component estimation was investigated: the filter type—Al against PMMA—at comparable beam spectra, the need for background de-trending prior to noise decomposition and spatial stationarity of the noise components over the image plane.

2. Background

Analysis of noise components in digital radiographic images is based on a linear-system analysis using noise samples obtained from homogeneously exposed images where noise

properties are assumed shift invariant (Williams *et al* 1999, Albert and Maidment 2000, Cunningham 2000). A simple three-parameter polynomial model has been proposed to describe the image noise as a function of detector x-ray fluence (Q) or detector air kerma (DAK) (Borasi *et al* 2003, Burgess 2004, Bouwman *et al* 2009). Noise within the image is assigned to one of three sources (electronic, quantum and fixed pattern), depending on its signal dependency. Electronic noise is assumed to be stochastic additive signal, independent of Q, arising from pixel dark current shot noise, noise fluctuations on the gate and data lines in the readout process and amplifier noise (Siewerdsen *et al* 1997). It should be noted that electronic noise may have a fixed pattern (FP) component arising from offset variations in row/column or pixel amplifiers/switches. The magnitude of FP electronic noise is however a small part of the electronic noise and is generally removed by flat fielding. In this study, a further distinction has therefore not been made and FP electronic noise was simply included in the FP noise component as defined below. The variance due to quantum signal variations, assuming Poisson statistics, scales with Q (Rimkus and Baily 1983). Structured or FP noise is a superimposed, unwanted static signal due to structural detector response fluctuations, variations in pixel-to-pixel sensitivity or linearity, dead pixels and large area non uniformities from the x-ray beam (heel and geometric effects). The FP variance has a Q^2 dependence (Scheibe and Thomas 1981, Burgess 2004). In DR, the effect of FP noise can be largely removed using a flat-fielding correction. In CR, the correction is currently only applied for non-uniformities caused by the scanning and light-collection process during the readout (Schnell *et al* 2012). According to these definitions, electronic noise dominates at low exposure while FP noise at high exposure.

The three noise components are uncorrelated and can simply be added (Barnes *et al* 1982, Mackenzie and Honey 2007).

$$S^2 = {S_e}^2 + {S_q}^2 + {S_{\mathrm{fp}}}^2 \tag{1}$$

where ${S_e}^2$, ${S_q}^2$ and ${S_{\mathrm{fp}}}^2$ are respectively the noise variances or NPS for each frequency bin due to electronic, quantum and FP noise sources. With the polynomial assumptions regarding exposure dependency, we can write

$$S^2 = k_e + k_q Q + k_{\mathrm{fp}} Q^2 \tag{2}$$

where fitting parameters k_e, k_q and k_{fp} respectively represent electronic, quantum and FP noise coefficients. The total un-normalized NPS, calculated from images linearized to number of photons per unit area (IEC 2005) can be written as (Nishikawa and Yaffe 1990):

$$NPS(f, Q) = NPS_e(f) + NPS_q(f, Q) + NPS_{\mathrm{fp}}(f, Q) \tag{3}$$

Applying the polynomial model gives

$$NPS(f, Q) = NPS_e(f) + NPS_q(f)Q + NPS_{\mathrm{fp}}(f)Q^2 \tag{4}$$

where $NPS_e(f)$, $NPS_q(f)$ and $NPS_{\mathrm{fp}}(f)$ are respectively the electronic, quantum and FP noise power spectra coefficients fitted for each frequency bin.

3. Materials and methods

3.1. Image acquisition

Six standard digital mammography systems were included in the study: five flat-panel detector based units and a computed radiography system (CR). Basic technical parameters for the detectors are given in table 1.

Table 1. Characteristics of the mammography detectors.

Detector name	Technology	Pixel pitch (μm)	Pixel matrix
Carestream SNP-M1	single-side needle CR	49	3584 × 4684
Fuji Amulet	a-Se/optical switch	50	3540 × 4740
GE Essential	CsI/a-Si TFT switch	100	2394 × 3062
Hologic Selenia Dimensions	a-Se/TFT switch	70	3328 × 4096
IMS Giotto	a-Se/TFT switch	85	2816 × 3584
Siemens Inspiration	a-Se/TFT switch	85	2658 × 3318

Images were acquired at the tube voltage and anode/filter combination selected by the AEC for 4 cm PMMA placed on the breast support table (grid in). The compression paddle and antiscatter grid were systematically removed from the mammography systems and the 4 cm PMMA block was suspended at the tube exit port. For the CR system, the storage phosphor plate was erased before data acquisition in order to avoid background radiation effects and was placed on the bucky table. All images were stored as 'FOR PROCESSING' DICOM data without post-processing. For the flat-panel detectors, images were corrected using the manufacturer's default flat-field calibrations (offset and gain corrections). Air kerma measurements were made with two dosemeters: a Radcal 9015 monitor (Radcal, Monrovia, USA) with a 6 cm^3 mammography ionizing chamber (10 × 5–6 M) and an RTI Barracuda (Mölndal, Sweden). Calibration of both devices was traceable to national standards. The air kerma was measured at the standard position, 6 cm from the chest wall edge and laterally centered, and then inverse-square corrected to give the air kerma at the detector surface (DAK). No correction was made for the transmission through detector covers. For each mammography unit, twenty flood images were acquired with open collimation at nine DAK levels, equally spaced by a factor of two. Target values were 6.25, 12.5, 25, 50, 100, 200, 400, 800 and 1600 μGy; the tube current-exposure time product (mAs) was varied to give the DAK closest to these values. When the target value could not be set with 4 cm PMMA, 1 cm of PMMA was added or removed to reach the lowest or highest DAK, respectively.

The filter material and thickness has to simulate the spectrum exiting an average breast. In mammography, a 2 mm thick Aluminum filter fixed at the output of the x-ray tube is recommended by the IEC standard (IEC 2005) and is therefore commonly used to acquire flood images for noise measurements. In a study for general radiography, Ranger *et al* (2005) showed that aluminum structure can add low frequency mottle and hence the use of ultra-high purity aluminum (>99.9% purity) in NPS estimation should be avoided. The influence of filtration type for mammography detectors was therefore compared in terms of noise components to the 4 cm thick cast PMMA block using a standard 2 mm thick Aluminium filter of 99.0% purity known to have some structure.

3.2. Response function

DAK values were converted to units of photon fluence (Q) by means of Boone's data (Boone 1998). Detector response curves were established from flood images using mean pixel value (PV) and photon fluence (table 2). A square area of 512 × 512 pixels at the centre of each image—including the reference dose point at 6 cm from the chest wall edge—was used for calculating the mean pixel value. The system response curves were fitted (weighted least square regressions with coefficients A, B and C) using linear or logarithmic equations (DR systems), or a power function expressed in a logarithmic scale (CR system).

$$PV = A + B \cdot Q \tag{5}$$

Table 2. Acquisition parameters and photon fluences, the response type and fit coefficients A, B and C for the response curves according to equations (5)–(7).

Detector name	Tube potential	Anode / filter	q_0 ($mm^{-2}\mu Gy^{-1}$)	Detector response curve	A	B	C
Carestream	28 kV	Mo/Mo	5167 (40 mm PMMA)	Log-arithmic	−2543	34 931	−1.2717
SNP-M1			4878 (30 mm PMMA)				
Fuji Amulet	29 kV	W/Rh	6189 (40 mm PMMA)	Log-arithmic	−3963	1051	-
			5957 (30 mm PMMA)				
GE Essential	29 kV	Rh/Rh	6275 (40 mm PMMA)	Linear	0	0.0012814	-
			5990 (30 mm PMMA)				
			6511 (50 mm PMMA)				
Hologic Selenia	29 kV	W/Rh	6189 (40 mm PMMA)	Linear	50	0.00047558	-
Dimensions			5957 (30 mm PMMA)				
IMS Giotto	28 kV	W/Ag	6734 (40 mm PMMA)	Linear	1.6	0.00065555	-
Siemens	29 kV	W/Rh	6189 (40 mm PMMA)	Linear	50	0.00058771	-
Inspiration			5957 (30 mm PMMA)				

$$PV = A + B \cdot \log Q \tag{6}$$

$$PV = A + B \cdot (\log Q)^C \tag{7}$$

3.3. Noise assessment (variance and NPS)

Before noise analysis, all pixel values were converted to photon fluence values using the detector response curves. For the CR detector, slight shifts in plate alignment during plate reading destroy the pixel-to-pixel correspondence of FP noise between successive CR images, leading to an underestimate of FP noise. Plate-specific maps of fixed pattern signal can be generated for a pixel-to-pixel gain correction in CR (Schnell *et al* 2012); we used the method of Illers *et al* (2004) in which each CR series for a given DAK and plate was spatially registered before noise calculation. The degree to which two CR images were spatially correlated was estimated using the cross correlation coefficient, computed between a reference image and the 19 successive images, for a shift range between −6 and +6 pixels in the horizontal and vertical directions. The shifts corresponding to the positions of the cross correlation peak were used to register the 19 CR images in each DAK series before noise calculation.

Each 512 × 512 ROI was shifted by 50 pixels between successive images for the 20 images at a given DAK level, starting from the image centre, ensuring that a fresh sample of FP noise was included in each ROI to improve ergodicity. In this way, average variance and NPS for the 20 different ROIs are presumed to provide an average noise estimation over many realizations of FP noise. If this were not done then noise averaged from a sequence of static ROIs on successive images (temporal average) may yield a different result from a spatial average over many ROIs performed on one image of the sequence (Dobbins 2000).

The large area spatial variations due to variations in signal from the heel effect and variations in x-ray path length through air are not representative of detector FP noise and hence should be removed before noise measurement (Dobbins 2000). For this reason, low-frequency signal trends were systematically removed by fitting and subtracting a 2D second-order polynomial to each 512 × 512 ROI before noise calculation.

The variance was then calculated by taking the arithmetic mean of the squared differences between each pixel value and the mean pixel value within the 512 × 512 ROIs. The NPS was

assessed as prescribed by the IEC protocol 62220-1-2 (IEC 2005). From each 512 × 512 ROI, nine spectra were averaged from 256 × 256 sub-ROIs, giving 180 spectra at each DAK level. The axial (0° and 90°) zero-frequency NPS components in the Fourier plane were systematically excluded to meet the assumption of spatial stationarity for noise measurements. This can further reduce FP noise such as the heel effect. This operation cannot be extended to the variance measurements, unless one calculates the variance by integrating the NPS. The averaged data from the 2D NPS were then rearranged in a radially averaged 1D vector as a function of spatial frequency.

3.4. Noise decomposition

In this section, the term *noise* and the variable S^2 are used for either the variance or the NPS for each frequency bin, referring to equations (2) or (4), respectively.

3.4.1. Polynomial method. Noise was decomposed using a second-order polynomial function of Q that was fitted to the noise data using least squares regressions. The treatment of uncertainties—and more specifically the weighting of the fitted data—can have a strong influence on the accuracy of the results, but as far as we know, this was not discussed in previous implementations (Borasi *et al* 2003, Burgess 2004, Bouwman *et al* 2009). Variance decomposition using equation (2) was therefore tested for each mammography system applying a least squared fit with weighted and unweighted data. The choice of weights was made such that each noise data provides equally precise information during the fitting. The error term minimized during the fitting was weighted as a function of the variability of noise data at the different DAK values by using a weight inversely proportional to the variance of the noise data at each dose level. This requires measurement of variance of the noise samples at each DAK (many images at each DAK). This weighting is based on the assumption that the weights are known exactly, but in practice this is never the case since an infinite set of noise measurements at a given dose level would be required. When the sample variance is not known with sufficient precision, estimated weights must be used instead—we suggest that photon fluence gives an estimate of the weighting instead of measured variance of noise. This choice of weights was tested and the precision of the fit compared. While investigating the fitting procedures, we also examined the use by some authors of squared fit coefficients in the polynomial equation ($k_e{}^2$, $k_q{}^2$ and $k_{\mathrm{fp}}{}^2$ in equation (2)) (Young *et al* 2006, Bouwman *et al* 2009).

3.4.2. Explicit method. The explicit method involves several steps with minimal assumptions regarding the signal dependency of the three noise components. The first step is to isolate the non-stochastic component of the noise. First, for a given DAK level, each 512 × 512 ROI was de-trended using a 2D polynomial and the total noise was calculated (S^2). An average ROI was then calculated from all twenty 512 × 512 ROIs at the given DAK. This average ROI was considered to represent the structured noise of the detector to some reasonable precision. Then, division of each of the twenty ROIs (on a pixel by pixel basis) by the averaged ROI suppressed fixed pattern (non-stochastic) noise of the detector ($S^2{}_{\mathrm{div}}$) (Aufrichtig *et al* 2001). This operation is the same to that used to remove background intensity variations by flat-field techniques (Kwan *et al* 2006, Schmidgunst *et al* 2007). Division was preferred to subtraction by the average image as the latter approach may add noise if there are small exposure variations among the images. The averaged image contains a fraction of stochastic noise correlated to each of the twenty images, hence $S^2{}_{\mathrm{div}}$ has to be corrected by the factor $N/(N-1)$ to give the stochastic noise ($S^2{}_{\mathrm{st}}$), where N is the

number of images. The choice of $N = 20$ images was sufficient to have a signal-to-noise ratio larger than 25 for the averaged image, even for the lowest DAK of 6.25 μGy, and to give an error in NPS due to the division of less than 1% (Aufrichtig *et al* 2001). The detector FP noise ($S^2{}_{\mathrm{fp}}$) was taken as the difference between total and stochastic noises:

$$S_{\mathrm{st}}{}^2 = \frac{N}{N-1} S_{\mathrm{div}}{}^2 \tag{8}$$

$$S_{fp}{}^2 = S^2 - \frac{N}{N-1} S_{div}{}^2 \tag{9}$$

Electronic and quantum noise are independent (stochastic) noise sources. Electronic noise is exposure independent and hence is present even in the absence of x-ray signal. One option in estimating electronic noise is to calculate this directly from dark images (acquired with a shielded detector), however pixel values close to zero may be strongly affected by truncation or rounding operations performed by the different systems, or by threshold operations necessary to avoid negative pixel values. Histograms of zero-dose images for the six systems involved in this study were not Gaussian distributed (Poisson-distributed noise tends to Gaussian noise for large samples) whereas this was the case for the images at the other DAK levels (data not shown). For this reason, a linear extrapolation to stochastic noise data (S^2_{st}) in the low and middle dose range (6–100 μGy) was used to find the electronic noise component. The linear fit for electronic noise was made using weights equal to the inverse of the variance of the noise data at each DAK. Quantum noise was taken as the residual stochastic noise after subtracting the electronic noise component.

$$S_e{}^2 = \lim_{Q \to 0} S_{\mathrm{st}}{}^2(Q) \tag{10}$$

$$S_q{}^2 = S_{\mathrm{st}}{}^2 - S_e{}^2 \tag{11}$$

3.4.3. Quantum limited range. The quantum limited range is defined as the exposure range in which the quantum noise component is greater than the electronic or FP noise components. Using the polynomial decomposition method, the limits of this range can be easily calculated from the ratios between the noise coefficients:

$$\frac{k_e}{k_q} < Q < \frac{k_q}{k_{\mathrm{fp}}} \tag{12}$$

3.5. Noise stationarity

Spatial stationarity of noise after 2D second-order polynomial de-trending was measured by calculating noise maps across the image plane using $5 \times 5\,\mathrm{mm}^2$ ROIs spaced with a pitch of 10 pixels in both directions in space. For the sake of comparison between the systems, the standard deviation was normalized by the standard deviation measured in a $5 \times 5\,\mathrm{mm}^2$ ROI at the centre of the images. Variance for each $5 \times 5\,\mathrm{mm}^2$ ROI was then decomposed by applying the explicit method (with weighted least square regressions) described in section 3.4. The fraction of total noise for a given noise component was calculated by dividing the variance for the component by total variance, on an ROI by ROI basis.

Table 3. Quantum (k_q), electronic (k_e) and FP (k_{fp}) noise coefficients according to equation (2) for the polynomial noise decomposition obtained for different weighted least square regressions, mean and maximal deviations between the measured points and the fitted curves.

Detector name	Weighting	Fit coefficients	k_q	k_e	k_{fp}	Mean absolute deviation [%]	Maximal deviation [%]
Carestream SNP-M1	1/Var(σ^2)	not squared	113.5	6.41e5	2.11e-5	3.1	8.0
	1/Q		95.0	2.27e6	2.61e-5	8.2	25.9
	None		77.1	1.22e7	2.83e-5	47.6	238.9
Fuji Amulet	1/Var(σ^2)	not squared	26.2	3.91e6	6.44e-6	11.7	69.4
	1/Q		23.4	4.32e6	7.12e-6	12.1	76.3
	None		20.3	5.36e6	7.78e-6	16.3	82.5
GE Essential	1/Var(σ^2)	not squared	27.3	2.17e6	6.61e-7	2.2	4.3
	1/Q		28.6	2.03e6	4.06e-7	2.4	5.1
	None		29.9	1.17e6	2.69e-7	7.1	28.1
Hologic Selenia	1/Var(σ^2)	not squared	149.0	2.44e7	1.35e-5	1.4	7.3
Dimensions	1/Q		150.3	2.45e7	1.36e-5	1.6	6.7
	None		155.7	2.41e7	1.25e-5	2.2	5.4
IMS Giotto	1/Var(σ^2)	not squared	134.8	2.45e7	4.90e-6	0.7	2.2
	1/Q		136.0	2.44e7	4.57e-6	0.7	1.7
	None		135.9	2.44e7	4.59e-6	0.7	1.7
Siemens Inspiration	1/Var(σ^2)	squared	160.0	1.70e7	2.45e-11	7.7	38.4
		not squared	151.5	1.81e7	0.00	5.9	31.2
	1/Q		128.4	2.10e7	0.00	9.0	13.7
	None		117.6	4.34e7	0.00	31.9	104.1

4. Results and discussion

4.1. Response function

Tube potential and anode/filter settings selected by the AEC device for a 4 cm PMMA block used for the response curve and noise decomposition are given in table 2, with the fitted coefficients A–C in equations (5)–(7). A weighted method was required to achieve an accurate fit at low DAK. Averaged deviations between the measured mean pixel values and the corresponding fitted values were between 1.1% and 4.3% for the six mammography systems, with maximum deviations lower than 8.8%. The fitted equations were used to re-express the pixel values as units of photon fluence (Q) at the detector entrance.

4.2. Influence of polynomial fit method

Given that the noise data at each dose level have a different uncertainty, we expect that using weights inversely proportional to the variance of the noise data would yield the most precise parameter estimates. The fitting data in table 3 confirm this, with the weighted least squares method giving the best mean precision (mean absolute deviation) and the lowest maximal deviation for three of the six detectors. Using the weighted method was necessary to achieve a sufficiently accurate fit at low DAK (below 25 μGy) and hence find the electronic noise component (see figure 1). The effect of using estimated weights is difficult to generalize, but the results obtained for the six detectors indicated that weights chosen to be equal to the inverse of the photon fluence did not significantly affect the regression analysis compared to exact weighting (table 3).

Using squared coefficients did not influence the proportions of noise sources when the non-squared method gave positive coefficients. For the Inspiration system, this avoided a negative second order (FP noise) coefficient but at the expense of precision (table 3). When the

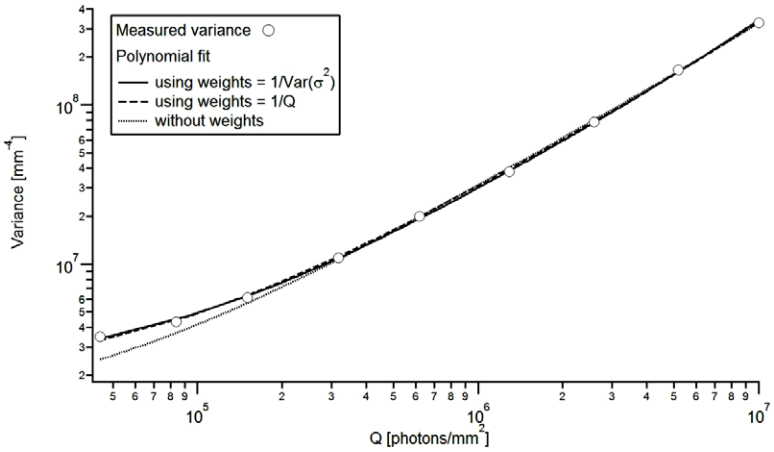

Figure 1. Influence of the polynomial fit method on the precision of the noise model (data: GE Essential).

non-squared method gives a negative coefficient, the fit using squared coefficient gives (positive) coefficients close to zero, for example $k_{fp} = 2.45 \times 10^{-11}$ for the Inspiration. It is of note that for the Siemens system, the negative second order coefficient did not mean that FP noise was not present; the reason was simply that the structured noise has a different dose dependency than assumed by the model. There does not appear to be a physical reason to square the coefficients—in fact negative coefficients can provide information on whether the three component model is suitable or valid for a given detector. A degree of consistency within the methods is also achieved by using non-squared coefficients for the variance and NPS fits (Mackenzie *et al* 2012). Practically, squared coefficients can be more difficult for the software to control during the fitting procedure; squared coefficients may be more sensitive to starting conditions.

4.3. Influence of de-trending

Variance decomposition performed without de-trending showed a FP noise that dramatically increased with ROI size and dose (figure 2). The variance compared to the integral of NPS calculated without the Fourier axes (Parseval's theorem) showed an increasing bias with the ROI size from very low frequency trends present in the image noise ($< 0.2\,mm^{-1}$). After 2D second-order polynomial fit subtraction the variance remained largely independent of ROI size and close to the integral of NPS. The use of an efficient de-trending method is therefore necessary to combine the higher statistical precision due to a larger ROI together with an accurate evaluation of variance. An optimal ROI size that corresponds to the best compromise should otherwise be used (Bouwman *et al* 2009). The European guidelines recommend an ROI size of $5 \times 5\,mm^2$ for variance analysis and this effectively places a lower frequency bound of $0.2\,mm^{-1}$. Results from this study suggest that even the $5 \times 5\,mm^2$ ROI tends to overestimate FP noise at high DAK compared to analysis with de-trending and this will subsequently affect fitted noise coefficients and the quantum limited dose range.

4.4. Influence of additional filter

Low frequency mottle in images acquired with the additional Aluminium filter resulted in an overestimation of the NPS at low spatial frequencies, especially below $0.5\,mm^{-1}$, compared to

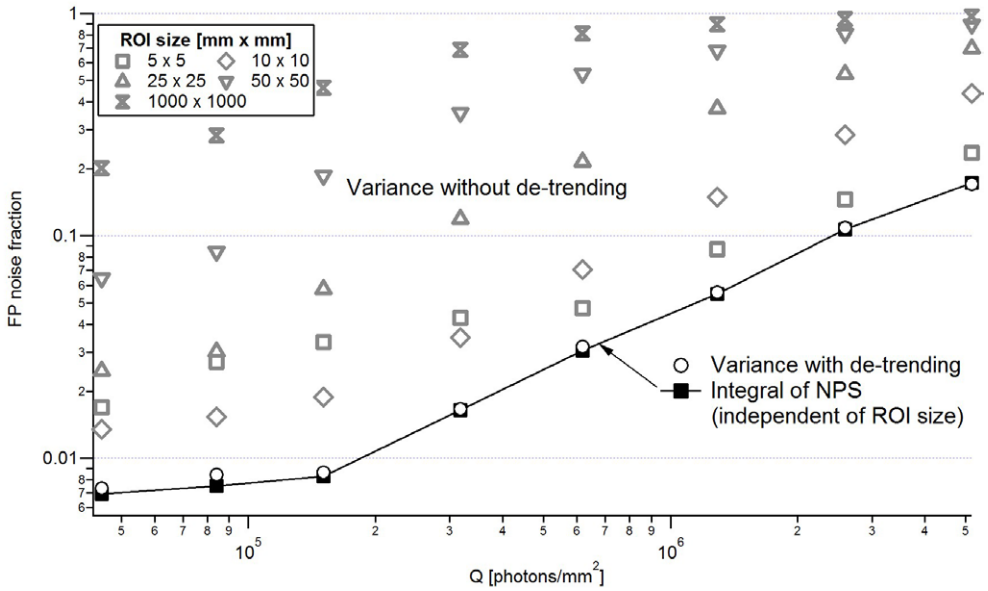

Figure 2. FP variance fraction measured as a function of ROI size without de-trending, and after the 2D polynomial de-trending. Comparison of the variance to the integral of NPS calculated as described in section 3.3 (data: GE Essential).

data from the PMMA images. These results were similar to those found for an RQA5 beam in conventional radiography (Ranger *et al* 2005). The noise decomposition in this work showed that 1) stochastic noise was not modified by the filter type and 2) FP noise was increased by an additional amount of structure coming from the Aluminum plate (figure 3). In this example, the polynomial method using the Al filter would give a quantum dominant range of 12.5–1450 μGy compared to 17.8–2720 μGy for the PMMA. De-trending was not entirely effective in removing this low-frequency structured mottle and a hence a PMMA filter would offer a more accurate representation of detector noise, compared to the Al plate used here (known to have structured noise). For QC measurements, the use of a PMMA filter is difficult given the practical difficulty of safely and quickly suspending the PMMA at the tube exit port. Before routine use of an Al filter in QC, we recommend that the filter should be checked for structured noise.

4.5. Noise decomposition

Figures 4(*a*)–(*f*) compare variance decomposition by the polynomial and explicit methods on the six digital mammography systems. In general, FP noise from the polynomial model corresponded to non-stochastic noise for the explicit decomposition method, while stochastic noise for the explicit decomposition equaled the sum of electronic and quantum noise from the polynomial model. However, some notable differences were seen, especially for FP noise. The explicit method showed that FP noise is not always proportional to photon fluence at the detector within all or part of the dose range tested. For the five DR systems, the deviation from proportionality is particularly noticeable at low DAK where FP noise reaches a threshold and does not decrease as rapidly as required by the polynomial model. For these systems, the polynomial decomposition underestimates FP noise at low DAK, sometimes by more than an order

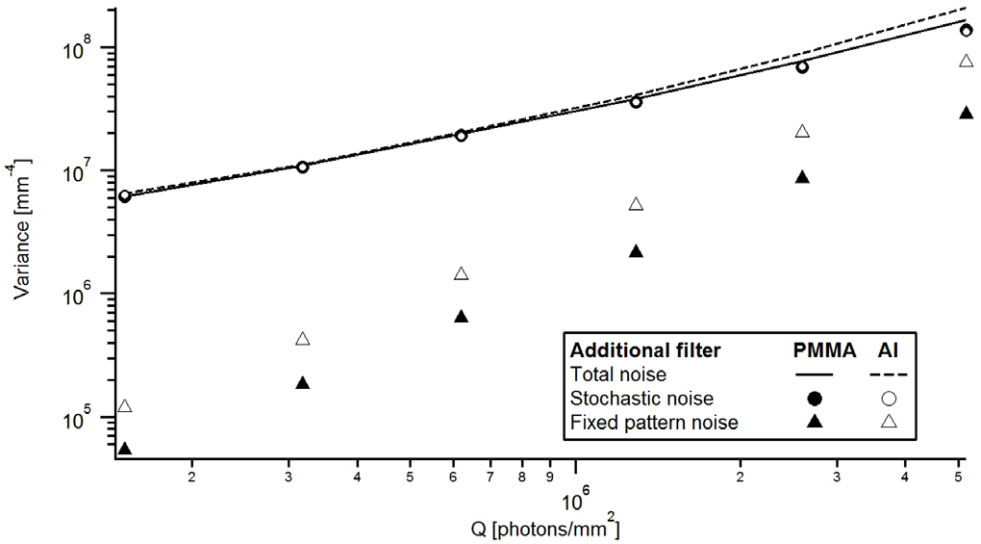

Figure 3. Influence of additional filter material on the noise components as a function of DAK (data: GE Essential).

of magnitude (GE Essential, IMS Giotto and Fuji Amulet at 6.25 μGy). The extreme case is for the Siemens Inspiration, where no FP noise is found by the polynomial method. However, because of the small fraction of FP noise at low DAK (less than 5% of total noise for a DAK below 25 μGy for all the systems), any error in FP noise estimation has only a limited impact on the total accuracy of noise component assessment if the polynomial method is used.

The discrepancy in FP noise at low DAK may arise from several reasons. Since the mask used for flat field correction is generated from several high dose x-ray images, as opposed to an ideal noise free condition, it contains a residual amount of stochastic noise that will add FP noise to the mammograms when the correction is applied. In (clinical) practice, even more deviations may occur. Variations in signal caused by the heel effect, x-ray path lengths through air, beam filter, compression plate and antiscatter grid will ideally be removed during the flat field correction. Since the flat fielding calibration is performed under one set of conditions, but images for noise analysis are acquired under another (e.g. differences in kV, target/filter material, grid in/out, PMMA thickness), differences in flat fielding geometries will generate structured noise. Moreover the flat fielding is generally based on the assumption that the detector responds linearly to exposure. The calibration of the flat field correction is done at one DAK, typically around 100 μGy. If the detector elements (dels) have a non-linear response, the two-constant (slope and intercept) correction applied in flat fielding will only operate properly under exposure conditions close to the calibration conditions. At low DAK, potentially different non-linearities of the del responses or of the gain correction for the readout electronics will result in image inhomogeneities measured as FP noise. Moreover, on images acquired at low DAK (< ~25 μGy) detector structures become visible—for example amplification steps, lines due to capacitive coupling between gate lines, defective lines/columns or clusters of pixel not properly corrected. These are structured noise components, yet are present in images acquired at DAK levels where electronic noise often forms the highest fraction.

For the Essential, Giotto and Selenia Dimensions, the two methods of noise decomposition showed close results for quantum and electronic variances, while for the other detectors,

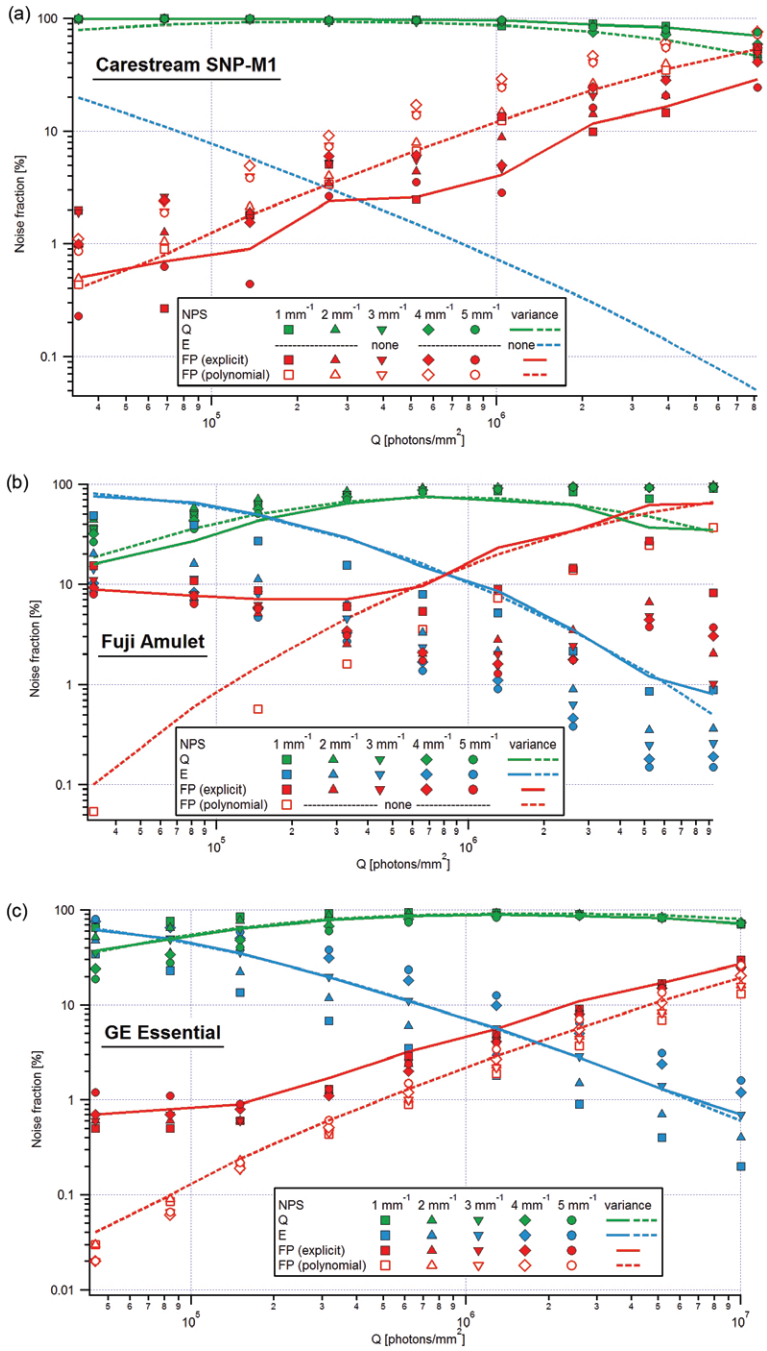

Figure 4. Fractions of the three noise components obtained with the explicit decomposition (filled symbols for the NPS and plain lines for the variance) and the polynomial decomposition (open symbols for the FP NPS and dotted lines for the variance). (*a*) Carestream SNP-M1. (*b*) Fuji Amulet. (*c*) GE Essential. (*d*) Hologic Selenia Dimensions. (*e*) IMS Giotto. (*f*) Siemens Inspiration (*Continued*).

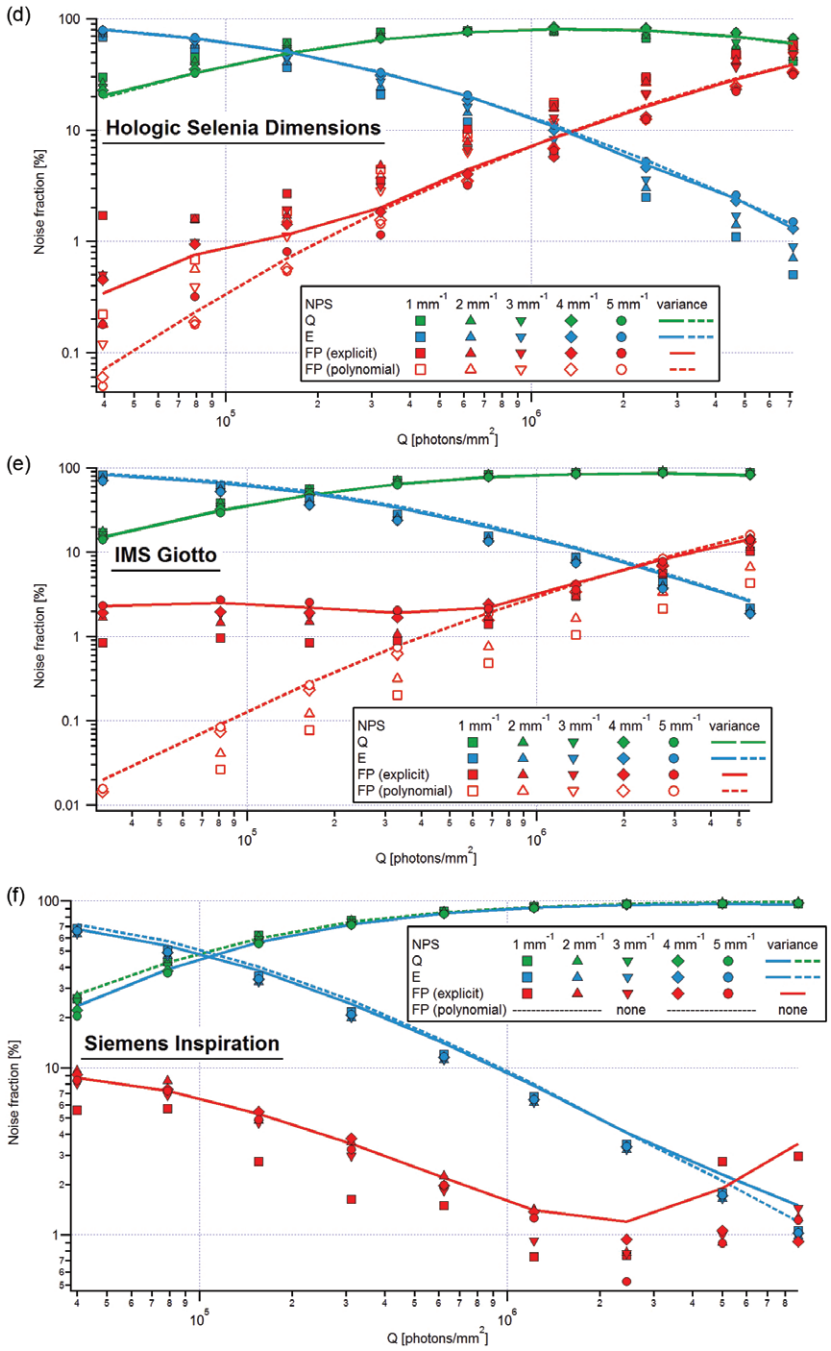

Figure 4. *Continued.*

the polynomial decomposition deviated over the entire DAK range. The polynomial decomposition gave a negative FP noise for the Inspiration. Forcing the second order coefficient to zero gave a good overall quality of the fit, except at high DAK where the polynomial decomposition yielded a quantum noise component higher than the total noise measured on the image (+22% at 800 μGy and +45% at 1600 μGy). For this system, FP noise deviated strongly from the behaviour expected with the polynomial model, constant below 200 μGy and with strong growth above 200 μGy. The Amulet showed quantum and FP noise components whose characteristics were far from those expected from the polynomial model. For this system, the filtering of 'FOR PROCESSING' data during the reading step may alter the raw image characteristics (Aufrichtig *et al* 2001, Rivetti *et al* 2009). For the CR system, the polynomial method gave a low (but non-zero) electronic noise component while the explicit decomposition found a stochastic noise strictly proportional to the photon fluence but no electronic noise. The polynomial decomposition gave a poor estimation of FP noise for the SNP-M1 with differences between −13 and +195% depending on DAK, and an underestimation of quantum noise (between −1% and −48% depending on DAK).

The generalization of the polynomial method from variance to NPS decomposition allows a direct comparison between the different noise components for systems with different pixel pitches, and has been described previously (Mackenzie and Honey 2007, Mackenzie *et al* 2012). Several other studies have used different analytical methods based on cascaded linear system analysis for NPS decomposition (Hillen *et al* 1987, Williams *et al* 1999, Evans *et al* 2002, Illers *et al* 2004, Al Tahli *et al* 2009). In this study, NPS decomposition agreed closely with variance decomposition (figures 5(*a*)–(*c*)). As for the variance, the polynomial method was likely to give a poor estimate of the FP NPS, especially an underestimate at low DAK. Figure 5(*c*) allows the comparison between the FP NPS calculated with the two decomposition methods for the target DAK of 100 μGy. For this DAK and with the exception of the Selenia, both methods gave systematically different FP NPS results. The differences in FP NPS are similar to those obtained for the variance decomposition, apart from the Amulet. The polynomial method gave a negative FP NPS for the Amulet except in the neighbourhood of the Nyquist frequency. This also occurred for the Inspiration over the entire spatial frequency range. For these two specific cases, the FP coefficient was forced to zero within the affected frequency range and the fit then gave results in close agreement with the explicit method for quantum and electronic components. This can be explained as FP NPS being just a small fraction of total noise. It has to be mentioned that the polynomial model applied on the NPS also failed to give reasonable values for quantum or electronic noise, in particular cases. The second-order polynomial fit sometimes diverged to meaningless values for low frequency NPS—this occurred for the quantum and electronic NPS below 0.5 mm^{-1} for the Essential, and for the quantum NPS for the Inspiration and Selenia (figures 5(*a*) and (*b*)).

The quantum NPS at zero frequency is determined by the quantum efficiency of the detector, and its shape is influenced by the square of the modulation transfer function (MTF^2) and the aliasing (Rabbani *et al* 1987, Granfors and Aufrichtig 2000). The correlation of light photons within the scintillator for the indirect conversion detector (GE Essential) results in a greater reduction of quantum NPS as a function of spatial frequency compared to the a-Se detectors (Samei 2003). The quantum NPS decreases much more quickly for the Amulet than for the other systems, which is surprising for an a-Se based system. One possible explanation is that filters applied during the readout result in a quantum NPS that does not represent the physical characteristics of this detector (Rivetti *et al* 2009).

Electronic noise is not correlated by the presampling MTF and we therefore expect this NPS to be white (Cunningham 2000). A pronounced low-frequency bump was however obtained for the Inspiration especially, the Giotto and to a lesser extent for the Selenia Dimensions. The electronic NPS was however measured from images acquired with the whole x-ray chain

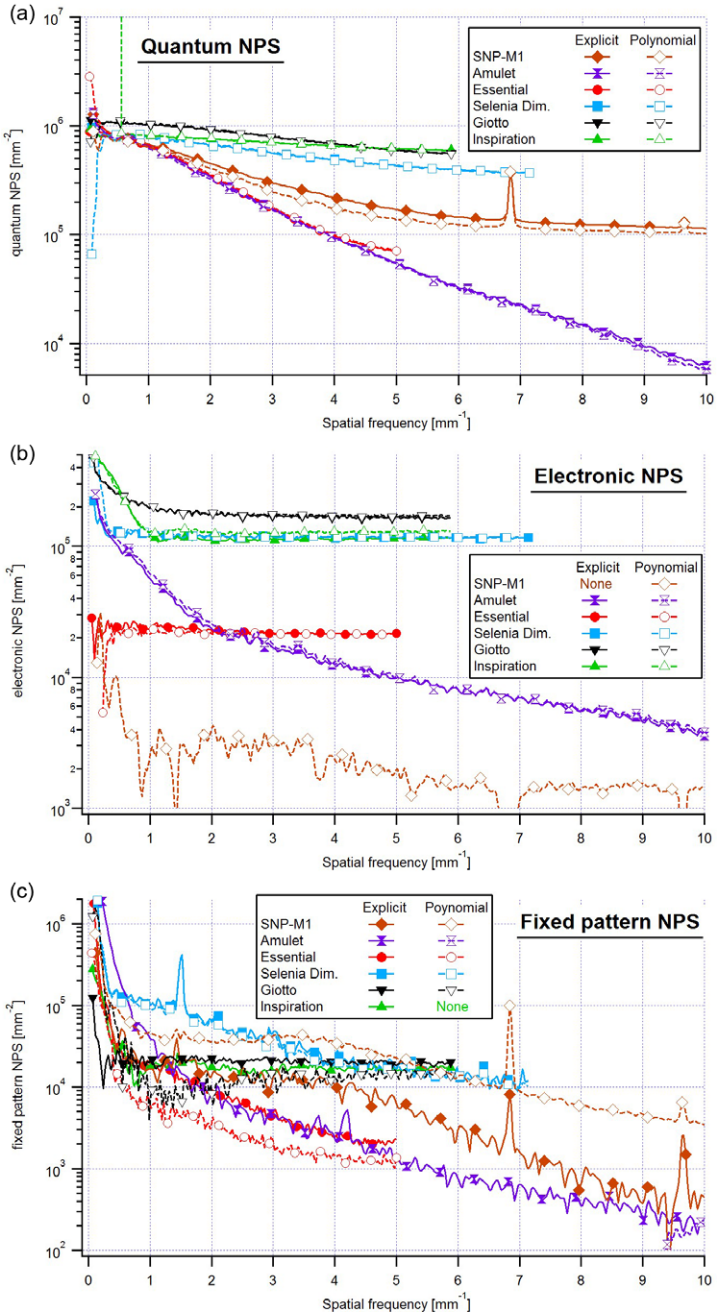

Figure 5. NPS components obtained with the explicit and polynomial decomposition methods for a target DAK of 100 μGy. (*a*) Quantum NPS. (*b*) Electronic NPS. (*c*) Fixed pattern NPS.

activated. An assessment of detector electronic noise alone would have needed measurements on raw dark frames. Once more, the shape of the electronic NPS for the Amulet indicates some correlation and hence probable post-acquisition filtering.

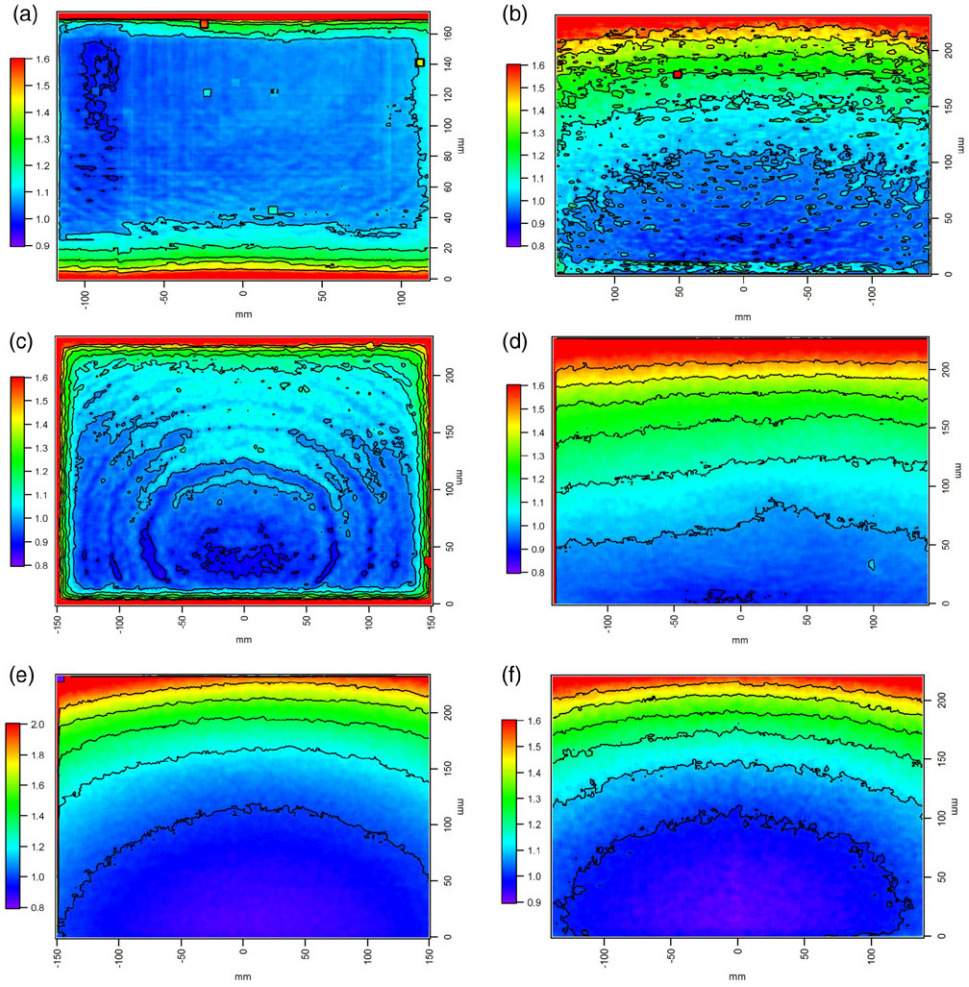

Figure 6. Maps of standard deviation using $5 \times 5\,\text{mm}^2$ ROIs spaced with a pitch of 10 pixels in both directions across the image plane, for a target DAK of $100\,\mu$Gy. The reference $5 \times 5\,\text{mm}^2$ ROI at 6 cm from the chest wall edge was used for normalization (target DAK = $100\,\mu$Gy). (*a*) Carestream SNP-M1. (*b*) Fuji Amulet. (*c*) GE Essential. (*d*) Hologic Selenia Dimensions. (*e*) IMS Giotto. (*f*) Siemens Inspiration.

The fixed pattern NPS shows various shapes reflecting intrinsic differences in converter materials, with more or less pronounced single spikes well localized in the frequency space. This corresponds to periodic signals in well-defined directions on the images (e.g. periodic lines). The systematic increase of FP NPS towards a peak at zero frequency is due to background trends incompletely corrected by the flat fielding.

4.6. Noise stationarity

The statistical description of a random process like image noise is determined by considering an ensemble of pixel values over a finite spatial area, often averaging several realizations that are spatially and/or temporally spaced. Efficient noise measurement therefore requires two conditions: stationarity and ergodicity. De-trending using the 2D polynomial subtraction

will reduce the large-scale image variations not explicitly related to the x-ray detector but not the complex spatial non-uniformities due to more localized signal variability. The European guidelines recommend a single small reference ROI of $5 \times 5\,\text{mm}^2$ localized at 6 cm from the chest-wall side for variance analysis.

Figures 6(*a*)–(*f*) show maps of standard deviation obtained for the mammography systems for a target DAK of 100 μGy. It can be seen that the noise is not nearly constant over the entire image plane, with higher levels in the periphery of the image plane compared to the regions usually covered by the breast. Noise generally increases from the chest wall side to the nipple side. For DR systems with flat fielding, this can be explained as follows. Without flat field correction, the PV would be ~30% higher at the chest wall edge due to the heel effect and variations in x-ray path length through air. The flat field correction is a multiplicative correction that applies the inverse of this shape to form the corrected image, increasing PV (and hence variance) at the nipple edge and reducing PV (and variance) at the chest wall edge (Marshall 2006). The ratio in standard deviation between the areas of highest and lowest noise in the image can easily reach a factor of two. However the area of the detector usually covered by the breast, which includes the ROI recommended by the Guidelines, is close to the average noise level of the image. The noise level in the ROI used by the Guidelines is thus representative of the noise level in the region typically occupied by the breast but should not be taken to represent noise over the whole image plane.

For all the systems involved in this study, the noise level pattern across the image plane varied with DAK, implying that the three noise components are both non-stationary and differently distributed across the image plane as DAK changes. A variance decomposition performed across the image plane was used to examine this phenomenon. Figure 7 compares mean noise fraction (the solid bar) measured across the whole image to the noise fraction measured in the $5 \times 5\,\text{mm}^2$ ROI used by the Guidelines (circular symbols) for the target DAK of 100 μGy (figures 7(*a*)–(*c*) respectively for the quantum, electronic and FP noise fractions). The error bars in these figures show the standard deviation for the noise fractions measured over the whole image. The three noise components are not stationary across the image plane for the six mammography systems. Quantum noise has systematically the least variation of the three noise components while FP noise has by far the highest variability, even for systems with flat fielding. Electronic noise stationarity is intermediate for the six mammography systems. A large range in quantum noise was found for the SNP-M1 and the Essential.

Figures 8(*a*)–(*f*) show some examples of the fractional noise components across the image for a target DAK of 100 μGy. For the Essential, the variability in quantum noise is due to particularly low values at the image sides and is not relevant for clinical regions (figure 8(*a*)). The CR system shows a quantum noise fraction varying between 20% and 100% along the direction perpendicular to the chest wall edge (figure 8(*b*)). This is different behaviour from that seen for the DR detectors, where quantum noise fraction is generally highest at the chest wall edge. For these detectors, the quantum noise fraction varies from side to side across the image plane, with the largest variation from 55%–85% for the Giotto (figure 8(*c*)). The Giotto showed the lowest spatial stationarity for the electronic noise fraction, varying between 15% and 40% of total noise depending on the location on the image (figure 8(*d*)). The FP noise fraction varies strongly in the image plane for the Selenia and SNP-M1. FP noise increases strongly at the edges of the image for the Essential but remains spatially uniform elsewhere on the image. For the Selenia, a random variation is superimposed to a low-frequency trend from side to side giving FP noise fractions between 2% and 10% across the whole pixel array (figure 8(*e*)). The SNP-M1 system has lowest stationarity for FP noise whose fraction varies from 10%–80% along the direction perpendicular to the chest wall edge (figure 8(*f*)). FP noise fraction is highest at the chest wall for the CR

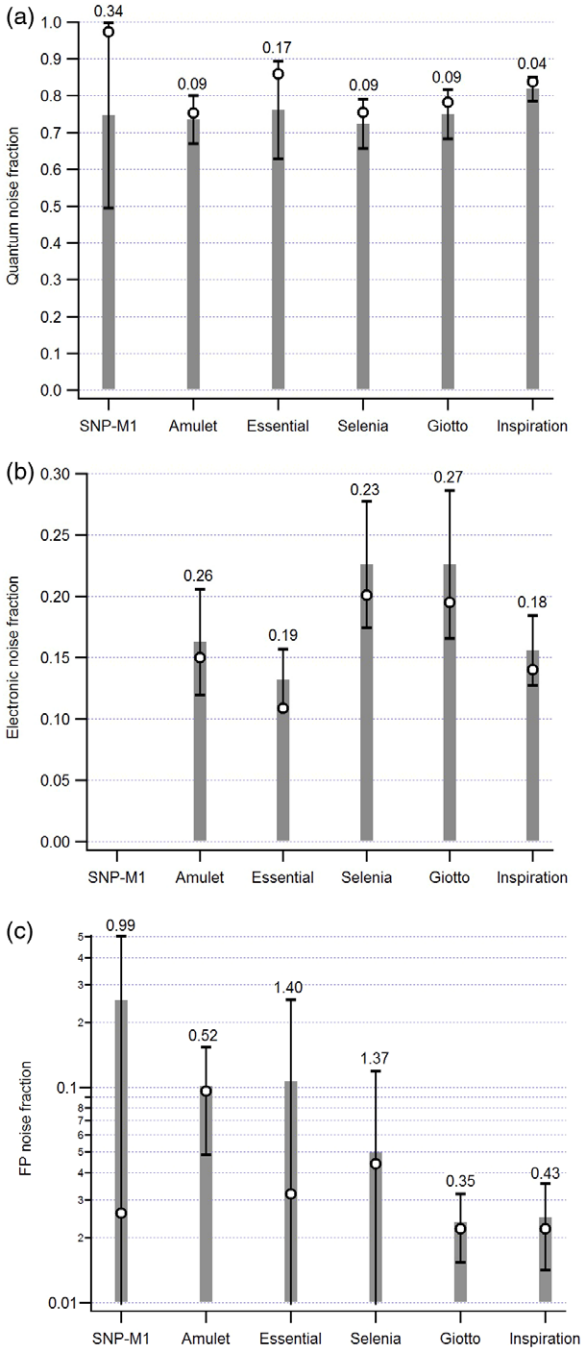

Figure 7. Mean fraction for the three noise components measured within $5 \times 5\,\text{mm}^2$ ROIs over the whole image plane (bars with error bars equal to ± one standard deviation and the coefficient of variation) and within the $5 \times 5\,\text{mm}^2$ reference ROI localized at 6 cm from the chest-wall side (circular points) for a target DAK = 100 μGy. (*a*) Quantum. (*b*) Electronic. (*c*) Fixed pattern.

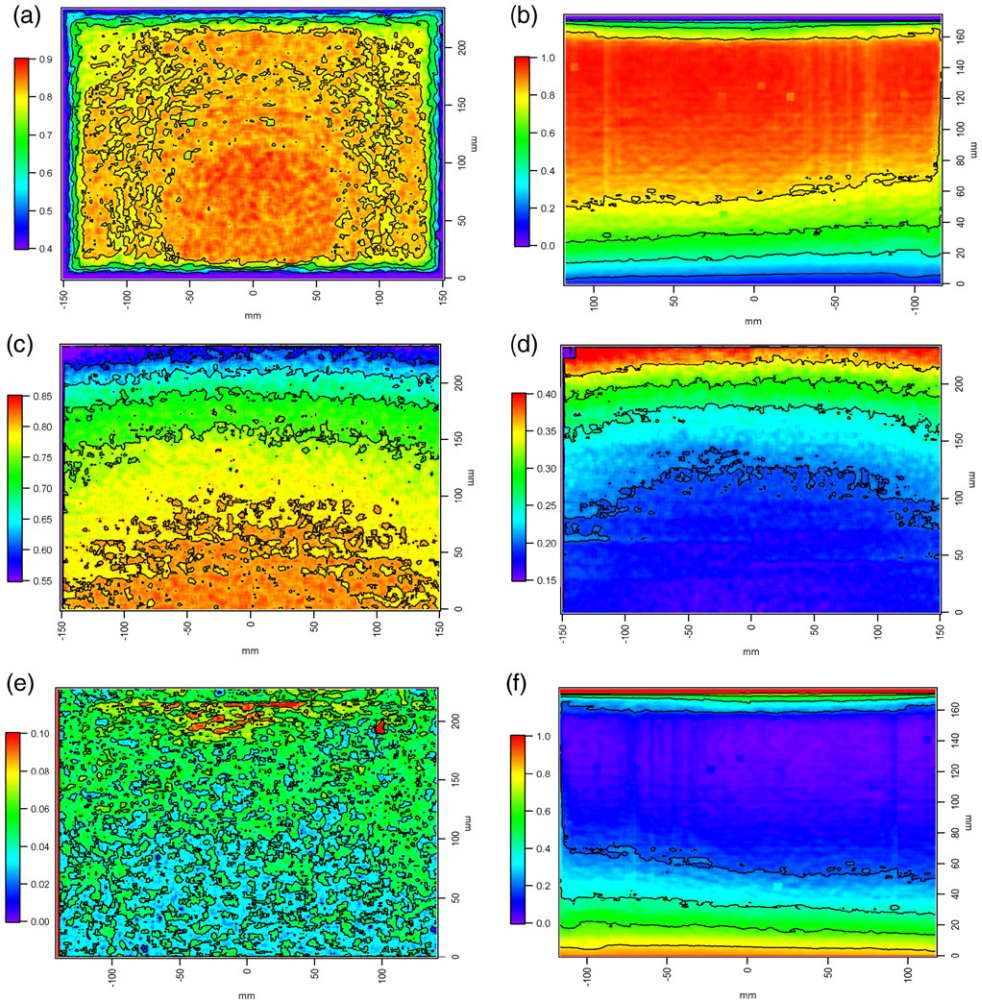

Figure 8. Fractional noise components across the image plane for a target DAK of 100 μGy. (*a*) Essential (quantum). (*b*) SNP-M1 (quantum). (*c*) Giotto (quantum). (*d*) Giotto (electronic). (*e*) Selenia Dimensions (fixed pattern). (*f*) SNP-M1 (fixed pattern).

system. This result may be explained by the absence of correction for structured signal for CR systems.

Returning to figure 7, the noise fractions measured within the Guidelines reference $5 \times 5\,\text{mm}^2$ ROI are given by the circular symbols in these figures. They are in most cases reasonably close to the mean noise fractions measured over the whole image plane (the bar in these figures). As already mentioned, differences seen for the Essential are due to the noise fractions at the sides of the images, distinctly different from the fractions measured throughout the remainder of the image, which is much more homogeneous. The large spatial variations in noise fractions for the CR system indicate that the fitted noise coefficients will depend strongly on the position and size of the ROI used for noise decomposition, which may in turn influence the quantum limited dose range. When determining noise coefficients, it is therefore important to use the same ROI for each measurement for a given DAK and in

the ensemble of measurements for different DAK settings. Results from this study suggest, however, that the ROI area and position recommended by the Guidelines will provide a good estimation of the averaged noise fractions across the important diagnostic regions of mammography DR detectors.

5. Conclusion

This study compared the commonly used second order polynomial model to give the quantum, electronic and fixed pattern noises against a more involved method that explicitly separated noise into these three components. The polynomial decomposition was often close to the explicit noise splitting method but occasionally failed to give accurate estimates of the different noise components. Furthermore, this method typically underestimated FP noise below 25 μGy and could generate negative noise coefficients in some cases. The polynomial model applied to the NPS could also give a sharp fall-off in a given noise component at low spatial frequencies or negative coefficients. The $5 \times 5\,\text{mm}^2$ ROI localized at 6 cm from the chest wall side as recommended for noise separation in the European Guidelines will give in most cases noise fractions relevant for the area covered by the breast but as we might expect, noise components may differ strongly from one location to another across the image plane. Spatial variations in noise components across the image plane also differ between systems: quantum noise was found to be the most stationary component whereas FP noise had the lowest stationarity, especially for the CR system. This study found that the accuracy and validity of the polynomial model can be improved by the use of weighted fits, an efficient de-trending method and optionally a PMMA filter rather than using Al. These limitations cannot be overcome when the system noise behaviour is far removed from that expected by the polynomial model; in this case explicit noise splitting is an option and could be performed for type test procedures or at acceptance tests.

References

Al Tahli A, Maack I, Koch A, Herrmann C, Medical Imaging 2009 and Physics of Medical Imaging 2009 A noise decomposition method for the image quality analysis of medical radiography detectors *Proc. SPIE* **7258** 72582P

Albert M and Maidment A D 2000 Linear response theory for detectors consisting of discrete arrays *Med. Phys.* **27** 2417–34

Aufrichtig R, Su Y, Cheng Y and Granfors P R 2001 Measurement of the noise power spectrum in digital x-ray detectors *Proc. SPIE* **4320** 362–72

Barnes G T 1982 Radiographic mottle: a comprehensive theory *Med. Phys.* **9** 656–67

Boone J M 1998 Spectral modeling and compilation of quantum fluence in radiography and mammography *Proc. SPIE* **3336** 592–601

Borasi G, Nitrosi A, Ferrari P and Tassoni D 2003 On site evaluation of three flat panel detectors for digital radiography *Med. Phys.* **30** 1719–31

Bouwman R, Young K, Lazzari B, Ravaglia V, Broeders M and van Engen R 2009 An alternative method for noise analysis using pixel variance as part of quality control procedures on digital mammography systems *Phys. Med. Biol*. **54** 6809–22

Burgess A 2004 On the noise variance of a digital mammography system *Med. Phys*. **31** 1987–95

Cunningham I A 2000 Applied linear systems theory physics and psychophysics *Handbook of Medical Imaging* vol 1 ed J Beutel *et al* (Bellingham, DC: SPIE) pp 79–159

Dobbins J T III 2000 Image quality metrics for digital systems physics and psychophysics *Handbook of Medical Imaging* vol 1 ed J Beutel *et al* (Bellingham, DC: SPIE) pp 161–222

European Commission 2006 The European protocol for the quality control of the physical and technical aspects of mammography screening: part B. Digital mammography *European Guidelines for Breast Cancer Screening* 4th edn (Luxembourg: European Commission) pp 105–65

Evans D S, Workman A and Payne M 2002 A comparison of the imaging properties of CCD-based devices used for small field digital mammography *Phys. Med. Biol.* **47** 117–35

Granfors P R and Aufrichtig R 2000 Performance of a 41 × 41 cm^2 amorphous silicon flat panel x-ray detector for radiographic imaging applications *Med. Phys.* **27** 1324–31

Hajdok G, Yao J, Battista J J and Cunningham I A 2006 Signal and noise transfer properties of photoelectric interactions in diagnostic x-ray imaging detectors *Med. Phys.* **33** 3601–20

Hillen W, Schiebel U and Zaengel T 1987 Imaging performance of a digital storage phosphor system *Med. Phys.* **14** 744–51

IEC (International Electrotechnical Commission) 2005 *Medical Electrical Equipment—Characteristics of Digital X-ray Image Devices: Part I. Determination of Detective Quantum Efficiency* IEC 62220-1-2 (Geneva: IEC)

Illers H, Vandenbroucke D and Buhr E 2004 Measurements of correlated noise in images of computed radiography systems and its influence on the detective quantum efficiency *Proc. SPIE* **5368** 639–47

Kwan A L C, Seibert J A and Boone J M 2006 An improved method for flat-field correction of flat panel x-ray detector *Med. Phys.* **33** 391–3

Mackenzie A, Dance D R, Workman A, Yip M, Wells K and Young K C 2012 Conversion of mammographic images to appear with the noise and sharpness characteristics of a different detector and x-ray system *Med. Phys.* **39** 2721–34

Mackenzie A and Honey I D 2007 Characterization of noise sources for two generations of computed radiography systems using powder and crystalline photostimulable phosphors *Med. Phys.* **34** 3345–57

Marshall N W 2006 A comparison between objective and subjective image quality measurements for a full field digital mammography system *Phys. Med. Biol.* **51** 2441–63

Nishikawa R M and Yaffe M J 1990 Model of spatial-frequency-dependent detective quantum efficiency of phosphor screens *Med. Phys.* **17** 894–904

Perry N, Broeders M, de Wolf C, Törnberg S, Holland R and von Karsa L 2013 *European Guidelines for Quality Assurance in Breast Cancer Screening and Diagnosis* 4th edn Supplements ed N Perry *et al* (Luxembourg: Office for Official Publications of the European Union) pp 21–2

Rabbani M, Shaw R and Van Metter R 1987 Detective quantum efficiency of imaging systems with amplifying and scattering mechanisms *Opt. Soc. Am. A* **4** 895–901

Ranger N T, Samei E, Dobbins JT III and Ravin C E 2005 Measurement of the detective quantum efficiency in digital detectors consistent with the IEC 62220–1 standard: practical considerations regarding the choice of filter material *Med. Phys.* **32** 2305–11

Rimkus D and Baily N A 1983 Quantum noise in detectors *Med. Phys.* **10** 470–1

Rivetti S, Lancelli N, Bertolini M, Borasi G, Golinelli P, Acchiappati D and Gallo E 2009 Physical and psychophysical characterization of a novel clinical system for digital mammography *Med. Phys.* **36** 5139–48

Samei E 2003 Performance of digital radiography detectors: factors affecting sharpness and noise *Advances in Digital Radiography* (Oak Ridge, TN: RSNA Education Center) pp 49–61

Saunders R S Jr, Baker J A, Delong D M, Johnson F P and Samei E 2007 Does image quality matter? Impact of resolution and noise on mammographic task performance *Med. Phys.* **34** 3971–81

Scheibe P O and Thomas A J 1981 Noise sources in digital fluorography *Proc. SPIE* **314** 202–9

Schmidgunst C, Ritter D and Lang E 2007 Calibration model of a dual gain flat panel detector for 2D and 3D x-ray imaging *Med. Phys.* **34** 3649–64

Schnell E A, Samei E and Dobbins J T III 2012 Plate-specific gain map correction for the improvement of detective quantum efficiency in computed radiography *Med. Phys.* **39** 1495–504

Siewerdsen J H, Antonuk L E, el-Mohri Y, Yorkston J, Huang W, Boudry J M and Cunningham I A 1997 Empirical and theoretical investigation of the noise performance of indirect detection, active matrix flat-panel imagers (AMFPIs) for diagnostic radiology *Med. Phys.* **24** 71–89

Warren L M, Mackenzie A, Cooke J, Given-Wilson R M, Wallis M G, Chakraborty D P, Dance D R, Bosmans H and Young K C 2012 Effect of image quality on calcification detection in digital mammography *Med. Phys.* **39** 3202–13

Williams M B, Mangiafico P A and Simoni P U 1999 Noise power spectra of images from digital mammography detectors *Med. Phys.* **26** 1279–93

Young K C, Oduko J M, Bosmans H, Nijs K and Martinez L 2006 Optimal beam quality selection in digital mammography *Br. J. Radiol.* **79** 981–90